Measurement of the Λ Magnetic Moment*

D. A. Hill† and K. K. Li‡
Laboratory for Nuclear Science and Physics Department, Massachusetts Institute of Technology, Cambridge, Massachusetts 02139

and

E. W. Jenkins, § T. F. Kycia, and H. Ruderman ‖
Brookhaven National Laboratory, Upton, New York 11973

(Received 6 July 1971)

The magnetic moment of the Λ hyperon has been measured at the Brookhaven cosmotron. Polarized Λ hyperons were produced by (1.02 ± 0.015)-GeV/c π^+ mesons incident on a Be target in the reaction $\pi^+ + n \to K^+ + \Lambda$. After passing through a strong pulsed longitudinal magnetic field, the Λ decay and the K^+ were observed in parallel-plate spark chambers in which the decay proton and/or the decay π^- could stop to facilitate momentum measurement. The spark chamber was triggered by an electronic counter system where the K^+ mesons were identified by velocity, specific ionization, and decay. The precession of the Λ polarization was detected by observing the rotation of its asymmetric decay distribution projected onto a plane perpendicular to the Λ trajectory. Measurement of the direction and magnitude of the angle of rotation about the magnetic field direction gave the moment and its sign. Based on 3868 field-on events with an average value of the ratio $\int \vec{H} \cdot d\vec{l}/p_\Lambda$ of about 800 kG cm/(GeV/c), the magnetic moment of the Λ hyperon was found to be −0.73 ± 0.18 nuclear magneton.

I. INTRODUCTION

The intrinsic properties of elementary particles are the basic data for any further study of their classification and interactions. The magnetic moment, in addition to affecting the behavior of a particle in an external electromagnetic field, is closely related to the dynamic structure of the particle. It thus serves as one of the crucial tests for any complete theory concerning the particle and its interactions. Since the magnetic moments of the proton and neutron have been determined with great accuracy, it is a natural step to measure those of the remaining baryons. The Λ hyperon, with its relatively large production cross section, long lifetime, and distinctive decay pattern, is experimentally the simplest one to investigate.

Before the advent of the currently accepted unitary symmetry scheme, the Λ magnetic moment was calculated using various models for strong interaction.[1] Under unitary symmetry, the electromagnetic interaction of the baryon octet manifested itself in their mass splittings and magnetic moments. Although none of the models could predict the baryon magnetic moments *a priori*, they did predict relationships between them.[2-9] Some of the more definite results gave the Λ moment in terms of the well-known proton and neutron moments. Thus a precise measurement of the Λ magnetic moment can distinguish between some of the models.

The possibility of measuring the hyperon magnetic moments was pointed out by Goldhaber[10] and by Lee and Yang.[11] They noted that the angle of precession of the Λ magnetic moment in an external magnetic field can be determined by measuring the rotation of its decay distribution about the direction of the field. Thus this method requires a sample of polarized hyperons, a strong magnetic field, and an asymmetric decay distribution.

Strongly polarized Λ's produced at backward angles in the center-of-mass system at momenta around 1.02 GeV/c have been observed in the reaction $\pi^- + p \to \Lambda + K^0$,[12] and in the charge-symmetric reaction $\pi^+ + n \to \Lambda + K^+$.[13] Since parity is conserved in the strong interaction which produces the Λ's, the Λ polarization vector $\vec{S}_\Lambda$ must be initially in the same direction as the normal to the production plane, $\hat{n}$, defined as

$$\hat{n} = \frac{\vec{p}_{\pi\,\mathrm{in}} \times \vec{p}_\Lambda}{|\vec{p}_{\pi\,\mathrm{in}} \times \vec{p}_\Lambda|}\,, \tag{1}$$

where $\vec{p}_{\pi\,\mathrm{in}}$ and $\vec{p}_\Lambda$ are the momenta of the incoming π meson and Λ, respectively.

The covariant equation of motion of a particle with spin in an electromagnetic field has been discussed by several authors.[14] A four-vector polarization S may be defined which has a zero time component S_0 in the particle's rest frame. The space components are the usual polarization vector. In a uniform magnetic field $\vec{H}$ the equation of motion of the three-vector $\vec{S}$ for a spin-$\frac{1}{2}$ neutral particle

with momentum $\vec{p}$, energy $E=\gamma m$, and magnetic moment μ in units of $(e\hbar/2mc)$ is

$$\frac{d\vec{S}}{dt}=\mu\frac{e}{\gamma m}\left[(\vec{S}\times\vec{H})+\left(\frac{\vec{p}}{m}\cdot(\vec{S}\times\vec{H})\right)\frac{\vec{p}}{m}\right], \tag{2}$$

where e is the electron charge and $\hbar=c=1$. For the arrangement in this experiment, $\vec{p}$ and $\vec{H}$ were chosen to be parallel and so the equation of motion reduces to

$$\frac{d\vec{S}}{dt}=\mu\frac{e}{\gamma m}(\vec{S}\times\vec{H}), \tag{3}$$

which implies that the polarization vector precesses about the direction of $\vec{H}$ at a rate

$$\frac{d\epsilon}{dt}=-\mu\frac{e}{\gamma m}H. \tag{4}$$

Thus the total precession angle ϵ is

$$\epsilon=-\mu\,\frac{e}{m}\,\frac{m}{p}\int\vec{H}\cdot d\vec{l}, \tag{5}$$

where the integral is taken over the flight path of the particle. If the magnetic moment is measured in units of nuclear magnetons ($1\mu_N=e\hbar/2m_pc=3.153\times10^{-18}$ MeV/G), then Eq. (5) becomes

$$\epsilon=-\mu\,\frac{e}{m_p}\,\frac{m}{p}\int\vec{H}\cdot d\vec{l}. \tag{5'}$$

This shows that the polarization vector of the Λ going in the direction of the magnetic field will show a right-handed rotation about $\vec{H}$ if its magnetic moment is negative ($\vec{\mu}$ and $\vec{S}$ antiparallel).

The weak decay $\Lambda\to\pi^-+p$ is known to violate parity conservation. It can therefore be described by two complex numbers a and b corresponding to the $s_{1/2}$- and $p_{1/2}$-wave decay amplitudes. The normalized angular distribution of the decay π^- with respect to Λ-spin direction in the Λ rest frame is[15]

$$4\pi N(\theta)d\Omega=(1+\alpha\bar{P}\cos\theta)d\Omega, \tag{6}$$

where $\bar{P}$ is the Λ polarization averaged over the Λ production angle, and α is the Λ-decay asymmetry parameter

$$\alpha\equiv\frac{-2\,\mathrm{Re}(a^*b)}{|a|^2+|b|^2}. \tag{7}$$

Experimentally it is known[16] that $\alpha=-0.645\pm0.016$. Since the Λ is essentially completely polarized at the momentum and angle chosen for this experiment,[12] the angular distribution of the pions should show a large asymmetry.

There have been several previous experiments to measure the Λ magnetic moment, all based on this general method.[17-20] Preliminary results of the present experiment based on about half of the events have also been published.[21] In Sec. II of this paper a more detailed discussion of the design, construction, and operation of the experimental apparatus is presented. Section III covers the data analysis procedure and the results. The results are further discussed in Sec. IV.

II. EXPERIMENTAL METHOD

A. General Design Considerations

From Eqs. (5) and (6), the standard deviation $\Delta\mu$ in determining the magnetic moment is

$$\Delta\mu\propto\frac{1}{\langle Hl/p\rangle N^{1/2}\{1-[1-(\alpha\bar{P})^2]^{1/2}\}^{1/2}}, \tag{8}$$

where N is the total number of events, and $\langle Hl/p\rangle$ is the averaged value of $\int\vec{H}\cdot d\vec{l}/p$. It is clear that the Λ rate and the magnetic field intensity are the factors limiting the accuracy. Due to the small production cross section and short mean life of the Λ, a system with a short high-field magnet, a well-localized Λ source, and a detection system having good spatial and temporal resolution is preferable. A counter-spark chamber system was used. Because of the relative ease of detection, especially on the identification of the K^+ meson, the reaction $\pi^++n\to\Lambda+K^+$ was chosen. For convenience in analysis, the magnetic field was chosen to be longitudinal, i.e., along the direction of flight of the Λ.

Ideally, in order to minimize the geometrical systematic errors and to increase rates, the detection system should be axially symmetric about the beam and cover a large solid angle. However, to conform to this symmetry in the present experiment would require a very large detector to identify the K^+. A compromise was made by dividing the space into two halves about the beam, the upper half for Λ detection and the lower half for K^+ detection, so that this detector was moved up as close to the target as possible. A hole was made in the system to clear the intense incoming beam to minimize accidental background.

The dimensions of the precession magnet play a decisive role in the accuracy of the measurement. For a given homogeneous longitudinal magnetic field, the angle of rotation of the Λ polarization vector increases, but the Λ rate decreases with the length of the magnet d such that

$$\frac{\Delta\mu}{\mu}\propto\frac{e^{d/2L}}{d}, \tag{9}$$

where L is the Λ mean free path. The optimum choice of d to minimize $\Delta\mu/\mu$ is thus $d=2L$. For 550-MeV/c Λ, d is about 7.5 cm. Compromising between maximum solid angle and maximum achievable magnetic field strength, the magnet was

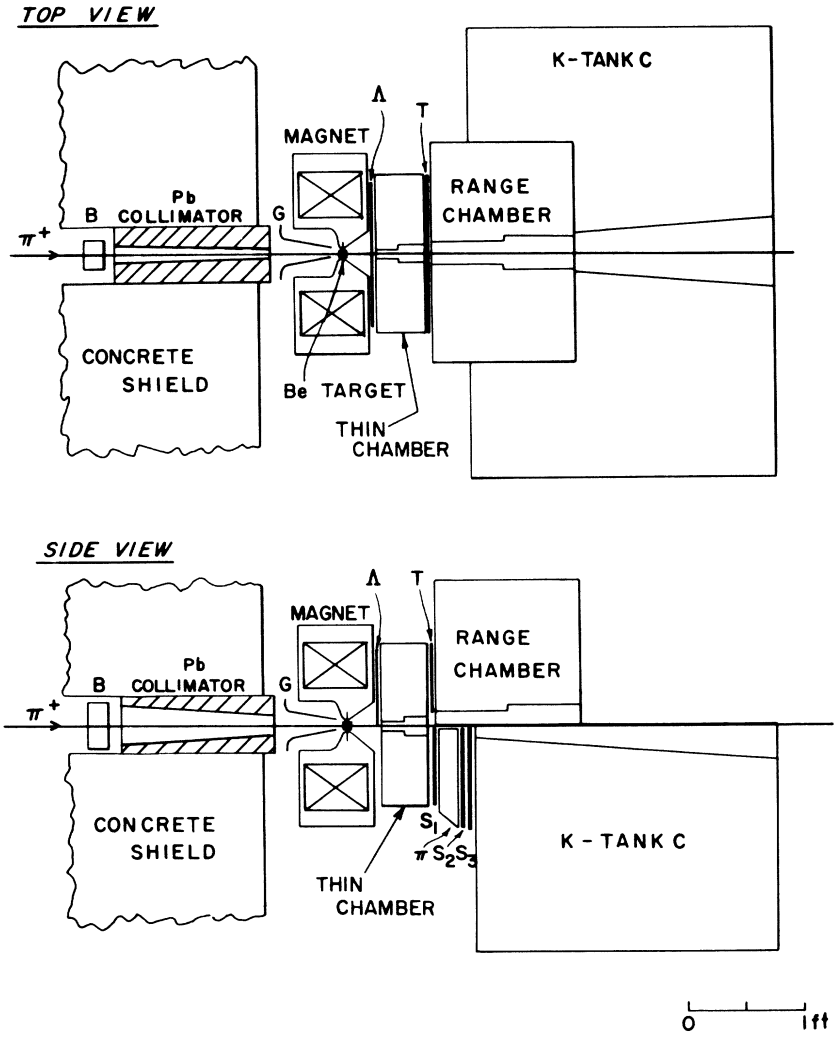

FIG. 1. General layout of apparatus.

made with a 60° conical bore. The diameter of the entrance end of the bore was again a compromise between the optimum beam focusing and maximum field and was made to accommodate a 2-cm-diam target. To minimize the effect of the uncertainty in the Λ production point, the target had to be much smaller than the magnet length d. Beryllium was used because of its relatively high content of loosely bound neutrons, and the known fact that it would not depolarize the Λ.[17]

B. Beam

The general layout of the experimental arrangement is shown in Fig. 1. The external proton beam from the cosmotron was focused on a $\frac{3}{8}\times\frac{3}{4}$-in.-cross section, 4-in.-long Cu target. The π^+ produced at a forward angle of 4°40′ passed through two momentum-analyzing stages giving a central momentum of 1.02 GeV/c, and were focused on the Be target. The beam was symmetric in design,[22] using two separate spectrometers; each consisted of a bending magnet and a quadrupole doublet (Fig. 2). The first spectrometer focused the object $T1$ onto a first focus $T2$ which was in turn focused by the second spectrometer onto $T3$ in such a way that $T3$ bore the same relationship to the second doublet as $T1$ to the first. Thus the momentum dispersion from the first half was compensated by the second half. A 2×2-in. brass slit was placed at $T2$ to define a ±1.5% momentum acceptance. The total intensity at the Be target was found to be about $2\times10^5/10^{11}$ internal protons at 2.2 GeV with a π^+/p ratio of about $\frac{1}{2}$. The beam profile was recorded by a 32-element semiconductor profile indicator.[23] The optimum image size was 1.55 cm vertical by 2.80 cm horizontal, and the angular divergences were calculated to be ±4.6° vertical and ±1.3° horizontal at the target.

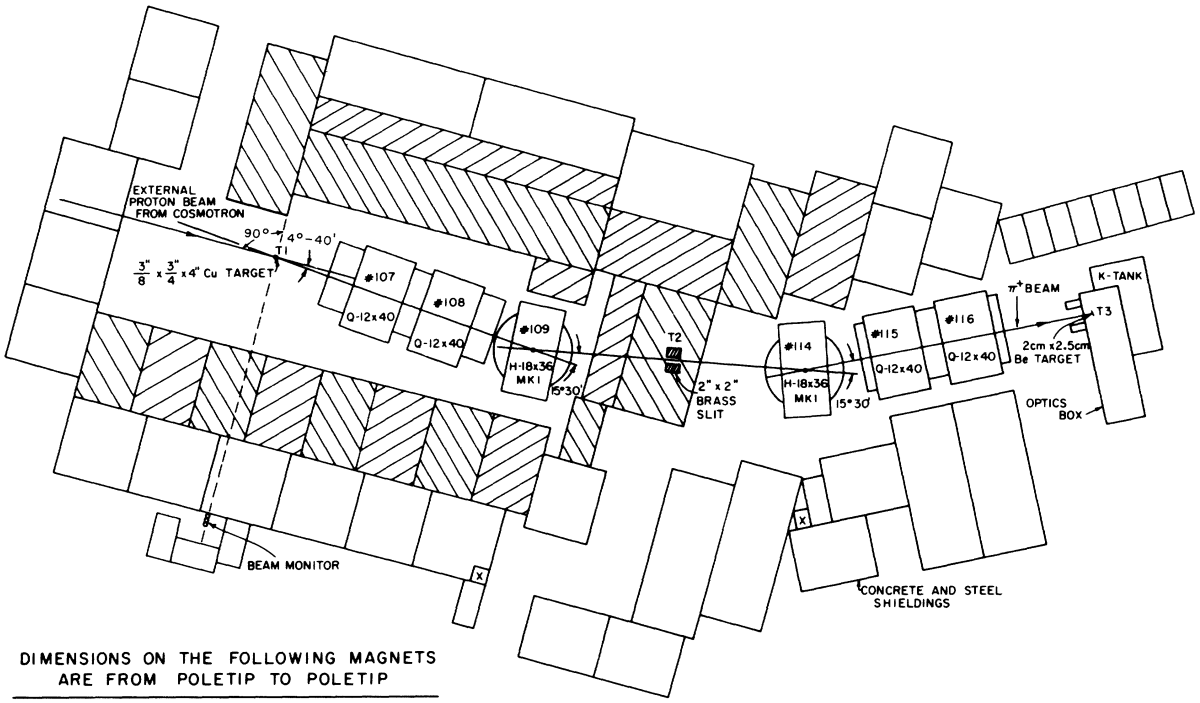

DIMENSIONS ON THE FOLLOWING MAGNETS ARE FROM POLETIP TO POLETIP

Cu TARGET	TO MAGNET 107	= 74"
MAGNET 107	TO MAGNET 108	= 15"
MAGNET 108	TO MAGNET 109	= $33\frac{1}{2}$"
MAGNET 109	TO MAGNET 114	= $168\frac{7}{16}$"
MAGNET 114	TO MAGNET 115	= $33\frac{1}{2}$"
MAGNET 115	TO MAGNET 116	= $15\frac{1}{16}$"
MAGNET 116	TO Be TARGET	= 74"

FIG. 2. Beam layout.

C. Precession Magnet and Target

The magnetic field was produced by a liquid-nitrogen-cooled pulsed magnet with a conical air core of 60° opening angle. It was a "flux concentrator" and worked, in principle, as a transformer with a single-turn secondary.[24] The field was monitored by two thin, long calibrated solenoids attached on the core surface so that their time-integrated signal gave a good approximation to the field integral. The voltage, current, and field integral pulses are shown in Fig. 3. The integrated output voltage at the time of the event, together with two fixed reference voltages and a polarity indicator, were displayed on an oscilloscope and photographed for each event. The magnet was mainly operated at a peak current of 3800 A at 400 V for 30–50 msec, of which 24–40 msec were flat enough to be used. The axial-field distribution is shown in Fig. 4. The field integral from the center of the target to the exit face was found to be independent of the polar and azimuthal angles to $\pm 2\%$. The total field integral $I(r)$ in kG cm along a line from the center of the target to a point a distance of r cm away could be fitted empirically by the following expression:

$$I(r) = \{138 + 43[1 - 1.48(7.5/r)^2 + 0.48(7.5/r)^3]\} V_0 , \tag{10}$$

where V_0 is the induced voltage from the calibrated solenoid, in volts. The polarity of the field was reversed frequently during the course of the experiment. The polarity was defined to be positive when the field was in the Λ direction of flight.

Because of the pulsed magnetic field, the target, which was located at the throat of the magnet, was built up of Be bars of $\frac{1}{8} \times \frac{1}{8}$-in. cross section insulated from one another to reduce eddy currents that could distort the field and give rise to large force on the target. It was cylindrical in shape, 2.5 cm long by 2 cm in diameter, with the upstream edge cut off so that Λ's originating from it would not pass partly through the magnet and enter the detection system.

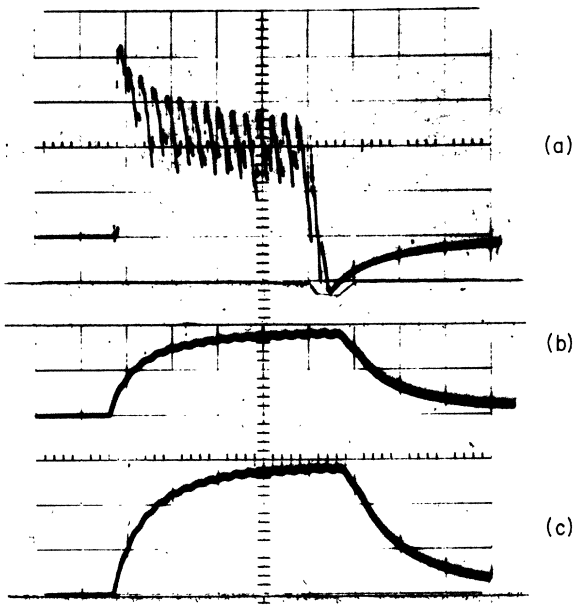

FIG. 3. Magnet pulse wave forms: (a) voltage pulse, (b) current pulse, and (c) field integral along core surface (horizontal scale: 1 msec/div).

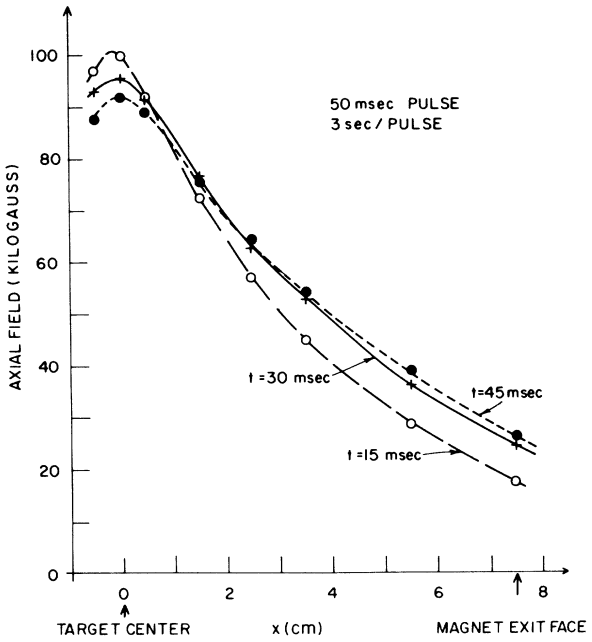

FIG. 4. Magnetic field distribution at various times during pulse.

D. Detectors

The π^+ mesons were identified by the beam counter B, a $2\frac{1}{2}\times 5$-in. cross section, 2-in.-thick threshold Cerenkov counter filled with FC75 and viewed by a 56 AVP photomultiplier through a water light pipe. Stray off-beam particles were rejected by the guard counter G. This guard counter G was a trumpet-shaped counter molded from $\frac{1}{4}$-in.-thick scintillator plastic in order to get as close as possible to the target. Though it was operated at liquid-nitrogen temperature in a region of about 40-kG pulsed magnetic field, no apparent change in pulse height was observed. The Λ produced in the upper hemisphere that survived two mean lives through the magnet entered the thin-foil chamber and decayed. They were selected by requiring a signal from the trigger counter T and no signal from the counter Λ placed immediately after and before the thin-foil chamber, respectively. Both counters Λ and T covered the entire upper hemisphere with such a relative geometry that the Λ counter completely shielded the T counter from the target. One or both of the charged decay particles entered the range chamber and stopped. The K^+ mesons entering the lower half of the thin-foil chamber were identified by ionization, velocity, and their decay into fast particles. These were accomplished by the π counter, the K^+ telescope counters S_1, S_2, S_3, and the K tank C. The π counter, subtending at the target a polar angle of 7°–40°, was a liquid threshold Čerenkov counter used to veto the fast π mesons. The 2-in.-thick radiator cell was divided into two halves at 20° with the inner and outer cells filled with FC75 and water, respectively, to compensate for the angular variation of the K^+-meson velocity. It was viewed by eight 6810-A photomultipliers and had a rejection ratio of ~10^4 for 1-BeV/c π mesons. The telescope counters S_1, S_2, and S_3 subtending 8°–40° polar angle at the target were used in dE/dx mode to further reject the minimum-ionizing π mesons. To compensate for the pathlength difference in the scintillator at different angles, the thickness of the scintillator was tapered radially at 1.5°. A correspondingly tapered Plexiglas piece was cemented with epoxy onto the scintillator to make a uniform thickness of 0.45 in. to improve light collection. The discriminators were set at 1.35 times minimum ionization. The fast-π-meson rejection for each counter was about two.

After traversing the chamber and the counters in front, the K^+ mesons entered the K tank C with a median momentum of about 500 MeV/c. The K tank was a semicylindrical water threshold Čerenkov counter, 30 in. long by 46 in. in diameter. It was used to stop the K^+ mesons and to identify them by detecting their fast decay products and to reject the slow protons. Ninety-five 6342-A photomultipliers were used, giving a photocathode-to-total-area ratio of about 4.3%. The signals from the tubes were added in groups of six and seven of

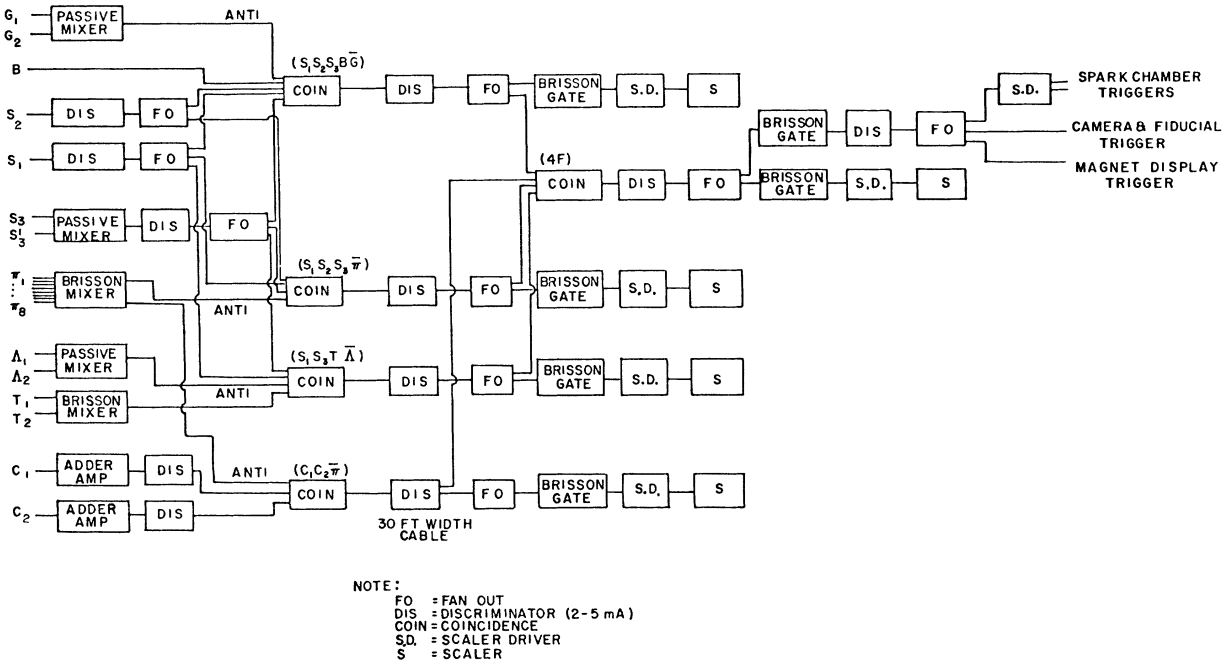

FIG. 5. Electronic block diagram.

equal gain to give sixteen outputs which were further combined into two groups, C_1 and C_2, by adder-amplifiers. C_1 and C_2 were required to be in coincidence to give the final signal C. The efficiency was about 55% for detecting K^+-meson decay and about 1.5% for counting 1-GeV/c protons.

E. Electronic Logic System

The arrangement of the electronic logic system using the Brookhaven nanosecond counting circuits[25] is shown in Fig. 5. The system consisted mainly of four circuits $(S_1S_2S_3B\bar{G})$, $(S_1S_2S_3\bar{\pi})$, $(S_1S_2T\bar{\Lambda})$, and $(C_1C_2\bar{\pi})$ in coincidence to give the final fourfold trigger $4F$ which triggered the spark-chamber system. On the K^+ side the coincidence $(S_1S_2S_3B\bar{G})$ assured a π^+ meson incident on the target giving a rather low-energy particle into the K^+ telescope while the coincidence $(S_1S_2S_3\bar{\pi})$ restricted the β of this particle to be smaller than 0.750 or 0.784, depending on its polar angle. On the Λ side the coincidence $(S_1S_3T\bar{\Lambda})$ occurred where one or more charged particles incident on the T counter were from a neutral particle decaying in the thin-foil chamber and were correlated with the low-energy particle on the K^+ side. These were then required to be in prompt coincidence. The coincidence $(C_1C_2\bar{\pi})$ indicated a slow particle incident on the K tank with a fast particle emerging, presumably from the K^+ decay. This signal was lengthened and timed in advance coincidence with the other three in the final coincidence $4F$ so that all K^+'s that decayed within about 3.2 mean lives were included. In order to reject prompt coincidences this signal was advanced by 0.5 mean lives (6 nsec). A fast turn-off gate was used to gate off all discriminators to prevent noise pickup from spark-chamber firing. A time-to-pulse-height converter was used with a multi-channel analyzer to record the time distribution of the K^+ decay signals from the K tank. The prompt coincidence on the K^+ side was taken as zero-time reference.

F. Spark Chamber and Optics

The spark-chamber system consisted of two different chambers: one 20-$\frac{1}{4}$-in. gaps, $14\frac{1}{2}\times14\frac{1}{2}$-in. cross-section thin-foil chamber located immediately next to the exit face of the magnet, and one 36-$\frac{1}{4}$-in. gaps, $14\frac{1}{2}\times21$-in. cross-section thick-plate range chamber following the thin-foil chamber. Both chambers had cuts subtending an angle of about 9° at the center of the target to clear the beam. The thin-foil chamber, which was used to observe the Λ decay and the K^+ meson, was constructed with 0.001-in.-thick Phosphor bronze foil tightly stretched on 1-in.-thick plate-glass frames. It provided relatively low density, good optical quality, high mechanical strength, and resistance to the eddy-current force induced by the pulsed magnet. The range chamber was made of six 0.063-in.- and fourteen 0.162-in.-thick aluminum plates and twenty-one 0.187-in.-thick brass plates cemented with epoxy on 1-in.-thick Plexiglas

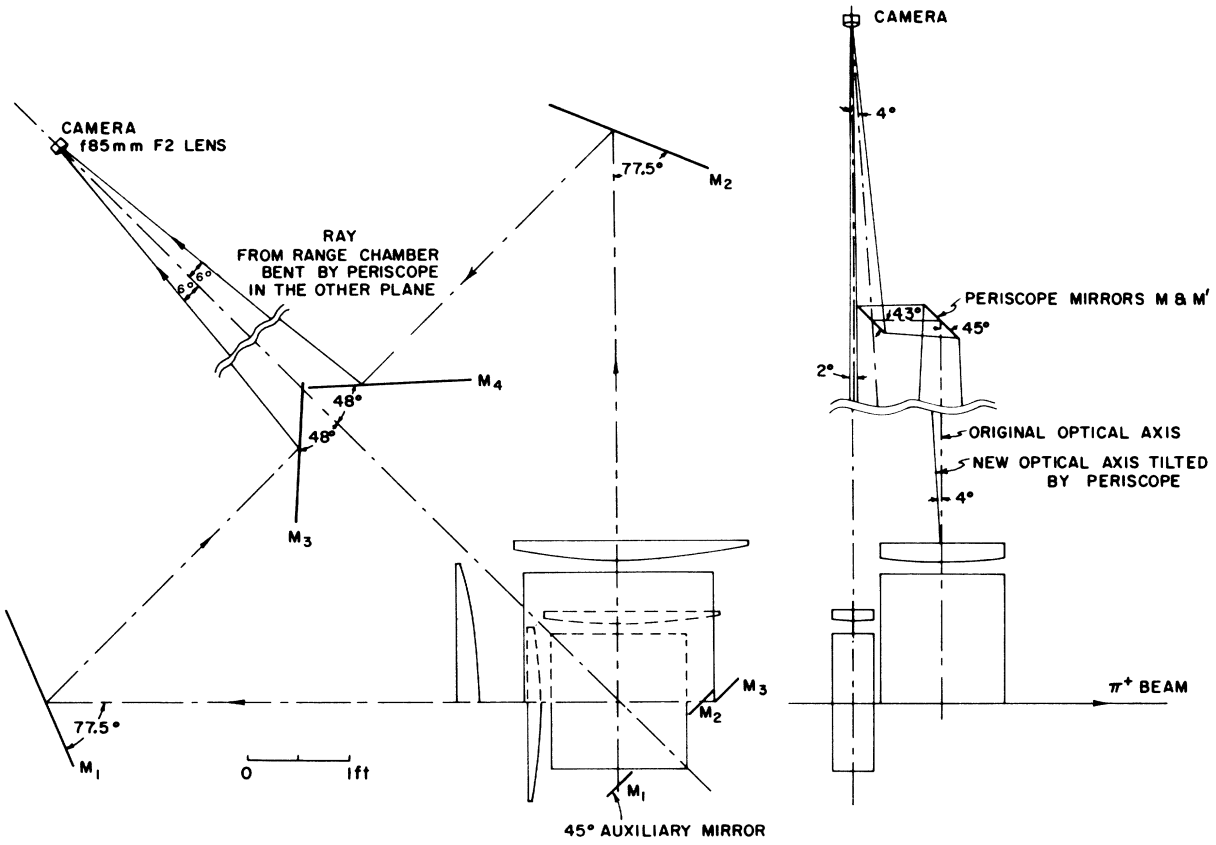

FIG. 6. Optics layout.

frames. It had enough material to stop 900-MeV/c protons and momentum resolution of about 3–5%, depending upon where the proton stopped. The chambers were flushed continuously with a 90% Ne–10% He gas mixture at slightly higher than atmospheric pressure. A high-voltage pulse was provided by triggered spark gaps operating at 8 kV with a capacity ratio of about $\frac{1}{3}$. The clearing field was adjusted to give a resolving time of about 0.25 μsec. L-shaped fiducial lights made from RCA 6977 lamps were mounted rigidly on the chambers. The pulsed magnetic field gave no adverse effect on the chamber performance.

The optical system was designed for minimum distortion in the thin-foil chamber and to bring the two 90° views of the two chambers into one full 35-mm film frame in such a way as to preserve the geometrical relationship in real space. A separate plano-convex Plexiglas field lens of 150-in. focal length was used on each chamber. The spherical aberration in the thin-foil chamber and the range chamber was about 0.5 mm and 1.3 mm, respectively. An 85-mm camera lens was operated at $f8$, giving the circle of confusion corresponding to ±7 in. depth of field to be about 0.5 mm. The general layout is shown in Fig. 6. Small 45° auxiliary view mirrors M_1, M_2, and M_3 were used to view the obscured regions behind the chamber beam holes. Calibration grids were photographed in chamber space before and after the experiment. The angular distortion in the thin chamber for a 60° track was about 1.5 mrad and was completely negligible. Kodak gray-base Shellburst 35-mm film was used. Photographed on the same film were a binary scalar, a decimal register, and the scope displays of magnetic field information.

G. Counting Rates

Singles rates on all counters were between 0.3 and 3 MHz, except on counters B and Λ which counted at near 30 MHz. These rates were not affected by the pulsed magnetic field. A 3-ft-thick concrete shielding and a molded Pb collimator were built between all counters and the last quadrupole to reduce background, especially in the K tank. The time distribution of the K-tank signal is shown in Fig. 7, where the same distribution without $\bar{\pi}$ and discriminations on the K^+ telescope is also shown for comparison. The tail of the distri-

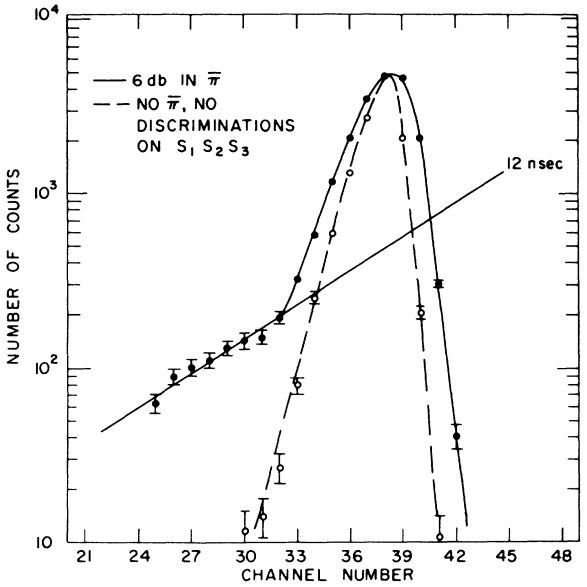

FIG. 7. Time distribution of the K-tank signals. The solid curve is from normal running, the dashed curve is without pion discriminations, and the straight line shows the proper K^+ lifetime. Horizontal scale is 1.8 nsec/channel.

bution fits the known K^+ mean life well. The triggering rate was 1/4 pulses at an average intensity of 0.5×10^5 π^+ on target. The rate of the observed Λ-like events, however, was about 1/70 pulses, or about 20/h. A large portion of the background triggers was due to interactions in the glass wall of the thin-foil-chamber beam hole. A coincident counter in front of the thin-foil chamber on the K^+ side reduced this background, but at the expense of events with small angle K^+. A short run without the target indicated that the Λ rate dropped by an order of magnitude.

III. ANALYSIS AND RESULTS

A. Scanning and Measuring

A total of 170 000 pictures were taken and manually scanned for events of the proper topology. A V-shaped pattern on the Λ side of the thin-foil chamber which pointed back to the target was the primary scanning criterion. These events were divided into two categories depending upon whether or not there was at least one straight-through track on the K^+ side. After the film had been scanned twice, 7660 events were accumulated. A typical event is shown in Fig. 8. These selected events were measured manually using an image-plane digitizer with least count corresponding to about 0.2 mm in real space. The auxiliary views were calibrated with their corresponding main views by

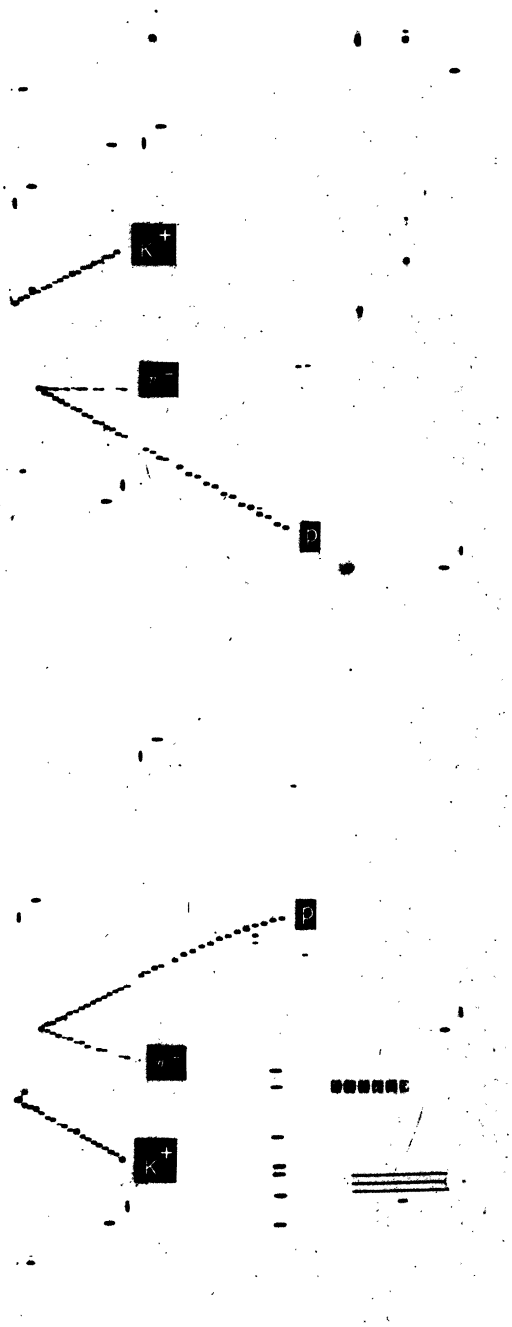

FIG. 8. A typical Λ event.

requiring those straight tracks appearing in both views to coincide. The fiducial positions were checked to within 1 mm in real space.

For each event, the four fiducials on the thin-foil chamber and the magnetic field display together with the reference voltages were measured. Three points on each track, of which at least two were in the thin-foil chamber, were measured to

assure good accuracy, as these were the points used to determine the corresponding straight line. Only the end point of the part of the track in the range chamber was measured. In the case where it scattered or interacted in the range chamber, an end point was located by projecting the observed end point along the chamber gap onto an extrapolated straight line from the thin chamber. These tracks and those emerging from the range chamber were flagged to have minimum range. For those tracks appearing in the small auxiliary views, special coding was used to correlate them.

B. Geometrical and Kinematical Reconstruction

The events were first analyzed using the information on the K^+ direction. This allowed the calculations of the neutron Fermi momentum and the reconstruction of the production plane. However, when this was compared with the production plane determined by using the Λ and beam directions only, it was apparent that there was a systematic shift due to the effect of the magnetic field on the K^+ trajectory. The events were then reanalyzed ignoring all K^+ information. When analyzed this way, no difference could be found between the events that had a K^+ track in the picture and those that did not. Both classes of events were used in determining the magnetic moment.

Each measured event was checked on geometry and on decay kinematics. Straight lines were fitted to the measured points in the thin-foil chamber. The geometry of the Λ-decay vertex was fitted subject to the constraint that the lines met at a point. The production point was taken as the point on the reconstructed Λ-decay plane that lay closest to the center of the target. The event was considered to originate from the target if this point was found to be within 0.4 cm from the target surface.

The decay kinematics were checked differently according to whether the range of either of the decay products was measured. If there was no range measurement, the Λ direction was taken along the line between the production point and decay point. From the angle between the Λ and its decay products the decay kinematics were determined. If a range had been measured, then the decay kinematics were determined from the momentum obtained from this range and the opening angle of the V. In this case the Λ direction could be recalculated and it was checked to see if the Λ came from within 0.4 cm of the target surface. Checks were also made to see that the particles which did not stop did not go farther than kinematically possible.

In approximately 3% of the measured events, the opening angle was so small that the data analysis program could not distinguish between the proton and the pion. In about half of these ambiguous cases one choice clearly gave a Λ momentum out of the range of production kinematics and so they could be resolved; otherwise they were discarded.

It was assumed that on the average the Λ polarization vector $\vec{S}_\Lambda$ was along the direction $\vec{p}_{\pi\,\mathrm{in}} \times \vec{p}_\Lambda$, where $\vec{p}_{\pi\,\mathrm{in}}$ was along the beam axis. For each event the field integral was calculated using Eq. (10). This assumed that on the average the Λ was produced at the center of the target.

Each event that could be analyzed was written on a magnetic tape. The events were flagged if the reconstructed Λ trajectory intersected the beam tube in the chamber. Also indicated on the tape was an event type: Type-1 events had no range determination on either decay particle, type-2 events had one range measurement, and type-3 events had both ranges measured. A total of 6018 events were accepted by the reconstruction program and written on the tape.

C. Selection of Events

Several cuts were made in the data to eliminate possible background or poorly reconstructed events. The Λ-decay vertex was required to be in the upper half of the thin-foil chamber, more than 7 cm downstream of the target center and within 20 cm of the beam axis. The Λ momentum vector was restricted to lie between 0.25 and 1.00 GeV/c and within 53° of the beam direction. A further kinematic cut was made on a quantity called the "effective mass squared." This quantity is calculated assuming the incident pion with a momentum of 1.02 GeV/c along the beam axis interacted with a stationary neutron to produce a Λ having the reconstructed momentum vector. Then the "effective mass squared" is the square of the missing mass calculated from the equation

$$M_{\mathrm{eff}}{}^2 = m_\Lambda{}^2 + m_n{}^2 + m_\pi{}^2 + 2[m_n E_{\pi\,\mathrm{in}} - E_\Lambda(m_n + E_{\pi\,\mathrm{in}}) + p_\Lambda p_{\pi\,\mathrm{in}} \cos\theta_\Lambda],$$

where θ_Λ is the angle between $\vec{p}_\Lambda$ and $\vec{p}_{\pi\,\mathrm{in}}$. The experimental distribution of this quantity should peak near the square of the K^+ mass. Events with $-0.10 \leq M_{\mathrm{eff}}{}^2 \leq 0.50$ (GeV)^2 were accepted.

After these cuts there remained a total of 5382 events, of which 2164 events had negative field, 2686 events had positive field, and 532 events had zero field. They could also be classified as 1400 events with no range determination (type 1), 2999 events with one range determined (type 2), and 983 events with both ranges determined (type 3).

The distribution of Λ-decay position, momentum, decay opening angle, and pion direction in the Λ center-of-mass system are shown in Figs. 9–13, respectively, along with the events generated in

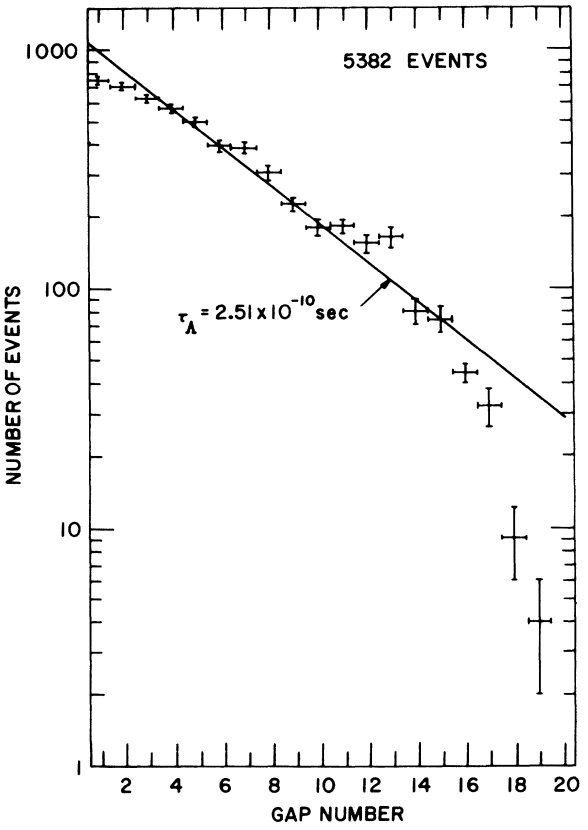

FIG. 9. Λ-decay vertex distribution along the beam direction for all accepted events. The gap width was $\frac{1}{4}$ in. The straight line was calculated using $\tau_\Lambda = 2.51 \times 10^{-10}$ sec and the observed mean momentum and angle.

a Monte Carlo simulation of the experiment. A discussion of the curves will be deferred until a description of the Monte Carlo calculation is given (Sec. III D).

D. Determination of Λ - Decay Asymmetry and Magnetic Moment

1. Decay Distribution

The polarization vector $\vec{S}_\Lambda$ in general made an angle κ with the magnetic field direction which, due to the target-neutron Fermi momentum, did not necessarily lie in the production plane as shown in Fig. 13. In the presence of the magnetic field $\vec{H}$, however, $\vec{S}_\Lambda$ precessed around $\vec{H}$ with an angular velocity independent of κ. Let $\vec{S}_\Lambda$ be precessed through an angle ϵ to a new vector $\vec{S}_\Lambda(H)$. As ϵ was measured in the xy plane normal to $\vec{H}$, it was convenient to look at the projected decay distribution on the same plane. Let η and η' be the projected angles between $\vec{p}_\pi$ and $\vec{S}_\Lambda$, $\vec{S}_\Lambda(H)$, respectively, onto the xy plane. According to Eq. (6), the distribution can then be written as

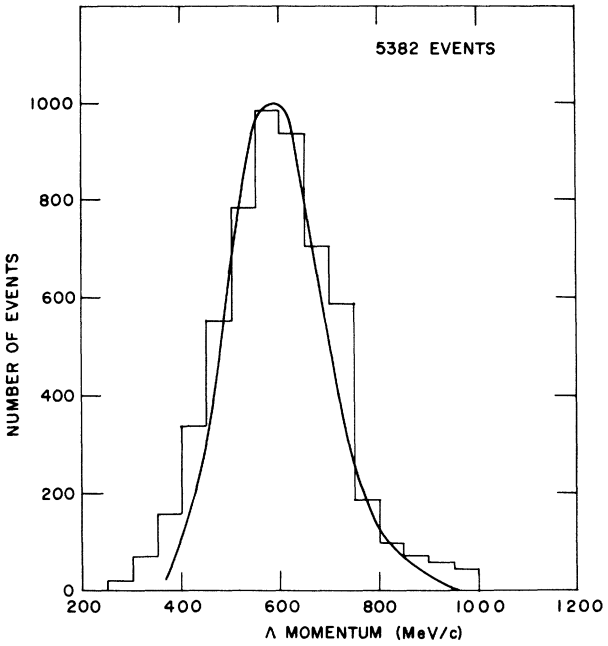

FIG. 10. Λ momentum distribution for all accepted events. The smooth curve was the Monte Carlo result.

$$4\pi g(\eta', \theta_\pi)d\Omega = [1 + \alpha\bar{P}(\cos\kappa\cos\theta_\pi + \sin\kappa\cos\theta_\pi\cos\eta')]\sin\theta_\pi d\theta_\pi d\eta', \quad (11)$$

where θ_π is the angle between $\vec{p}_\pi$ and $\vec{H}$. Thus the

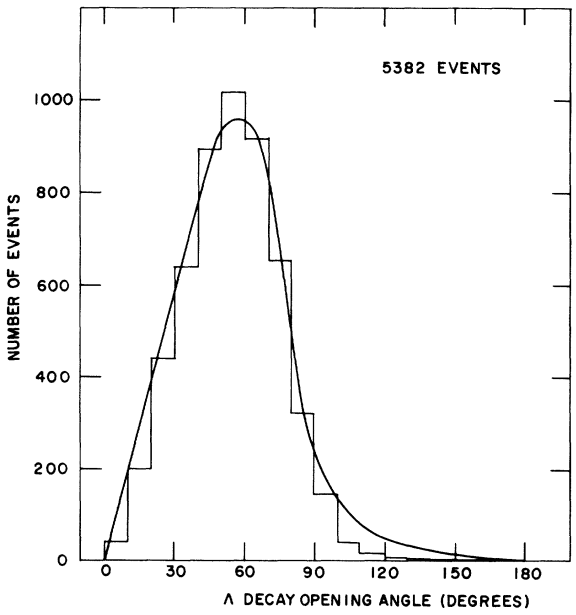

FIG. 11. Λ opening-angle distribution for all accepted events. The smooth curve was the Monte Carlo result.

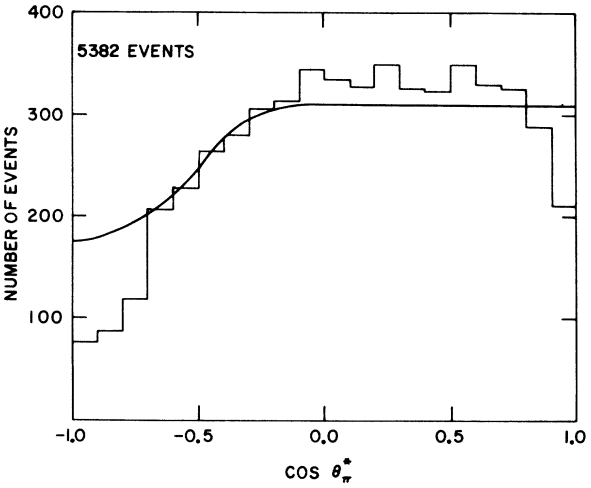

FIG. 12. The decay-pion angular distribution in the Λ center-of-mass system for all accepted events. The smooth curve was the Monte Carlo result.

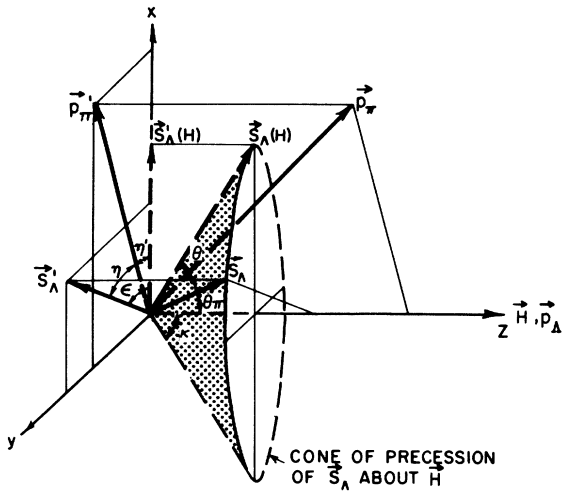

FIG. 13. Definition of angles in Λ rest frame used in analysis.

projected distribution is

$$f(\eta)d\eta = \frac{1}{2\pi}[1 + \tfrac{1}{4}\pi\alpha\bar{P}\sin\kappa\cos(\eta - \epsilon)]\,d\eta\,. \qquad (12)$$

The target-neutron Fermi momentum gave rise to a certain distribution in κ, which made the effective asymmetry constant $\alpha\bar{P}$ smaller. Equation (12) can thus be written as

$$f(\eta)d\eta = \frac{1}{2\pi}[1 + \tfrac{1}{4}\pi\langle\alpha\bar{P}\rangle\cos(\eta - \epsilon)]\,d\eta\,, \qquad (13)$$

where

$$\langle\alpha\bar{P}\rangle \equiv \alpha\bar{P}\langle\sin\kappa\rangle \qquad (14)$$

and $\langle\sin\kappa\rangle$ is the averaged value of $\sin\kappa$ over this distribution.

Because of the presence of the hole in the chamber, one of the decay particles from a Λ decaying near the surface of the beam tube could leave the chamber and would be missed in scanning. This constituted a bias in the decay distribution. For example, take the case of an event produced with the Λ going up and the K^+ going down. Then the normal to the plane of production is horizontal and to the right. If the Λ also decays in a vertical plane, then since the π^- in general makes a larger angle with the Λ direction than the proton, the event is more likely to be missed if the π^- goes down ($\eta = 90°$) than if it goes up ($\eta = 270°$). If the decay plane is horizontal ($\eta = 0$ or $180°$), however, there is no loss. Thus there is some depletion of events near $\eta = 90°$ and a smaller depletion near $\eta = 270°$. In order to account for this bias, a detection efficiency function $\beta(\eta)$ was calculated by a Monte Carlo method.

The projected angle distribution, Eq. (13), as modified by the efficiency function, is then

$$2\pi f(\eta)d\eta = \mathfrak{N}\beta(\eta)[1 + \tfrac{1}{4}\pi\langle\alpha\bar{P}\rangle\cos(\eta - \epsilon)]\,d\eta\,. \qquad (15)$$

The normalization factor $\mathfrak{N}$ can be determined from the condition

$$\int_0^{2\pi} f(\eta)d\eta = 1\,.$$

To do this the efficiency function was expanded in a Fourier series

$$\beta(\eta) = a_0 + \sum_{k=1}^{\infty} a_k\cos(k\eta - \delta_k)\,. \qquad (16)$$

Upon substituting into Eq. (15) and integrating, the normalization factor $\mathfrak{N}$ is

$$\mathfrak{N} = [a_0 + \tfrac{1}{8}\pi\langle\alpha\bar{P}\rangle a_1\cos(\delta_1 - \epsilon)]^{-1}\,. \qquad (17)$$

Note that the normalization is a function of both the average decay asymmetry $\langle\alpha\bar{P}\rangle$ and the magnetic moment.

2. *Monte Carlo Calculation of the Efficiency Function*

The efficiency function for detecting events by the apparatus was determined by using a Monte Carlo simulation of the experiment. The incident pion was given a momentum of 1.02 GeV/c along the beam axis and was allowed to produce Λ's from a neutron with Fermi momentum in the target. The production point was chosen at random from a uniform distribution throughout a target volume 2 cm in diameter and 2 cm long. The center-of-mass Λ production angle was chosen from a broken-line approximation to the measured[12] production cross section for the charge-symmetric reaction $\pi^- + p \to \Lambda + K^0$.

If either the Λ or the K^+ did not go in a direction that could be detected by the counters or spark chambers the event was discarded. The Λ-decay positions were chosen from an exponential distribution assuming a mean life of 2.62×10^{-10} sec. All Λ's decaying outside the thin-foil chamber were discarded. The velocity of the K^+ was checked to see that it was above threshold for the Čerenkov counter.

A second Monte Carlo program was written to read the tape containing the produced Λ's generated as described above and to choose the decay π^- and p from the unbiased distribution, Eq. (11). The parameters used in the decay distribution were $\langle\alpha\bar{P}\rangle = 0.69$ and $\mu_\Lambda = -0.75\mu_N$. The proportion of events with positive, negative, or zero field was chosen to be the same as in the data. For efficiency each produced Λ was allowed to decay ten times.

For each decay particle the point where it left the thin-foil chamber was calculated. From the exit point the program determined the number of gaps the particle traversed in the thin-foil chamber. If this number was less than three for either track, the event was discarded. Each accepted decay was written on a second tape in a format identical to the tape produced by the data analysis program. Thus the events could be selected using the same criteria as discussed in Sec. III C.

The selected Monte Carlo events were histogrammed into bins of 10° width in projected angle η. The ratio of accepted to generated events for each bin gave the efficiency for that range of projected angle. This raw bias was then passed through a quadratic smoothing program producing a smoothed bias function. It was verified that this smoothing did not affect the first two terms of the Fourier series expansion of the efficiency function. A sample of 20 000 generated decays of which 16 500 were accepted was used to calculate the efficiency functions. Typical distributions are shown in Fig. 14. The Fourier analysis of the efficiency function is summarized in Table I.

The data in Table I indicate that the a_1 coefficient is quite small, especially for the nonbeam-tube (NBT) event samples. As will be shown in Sec.

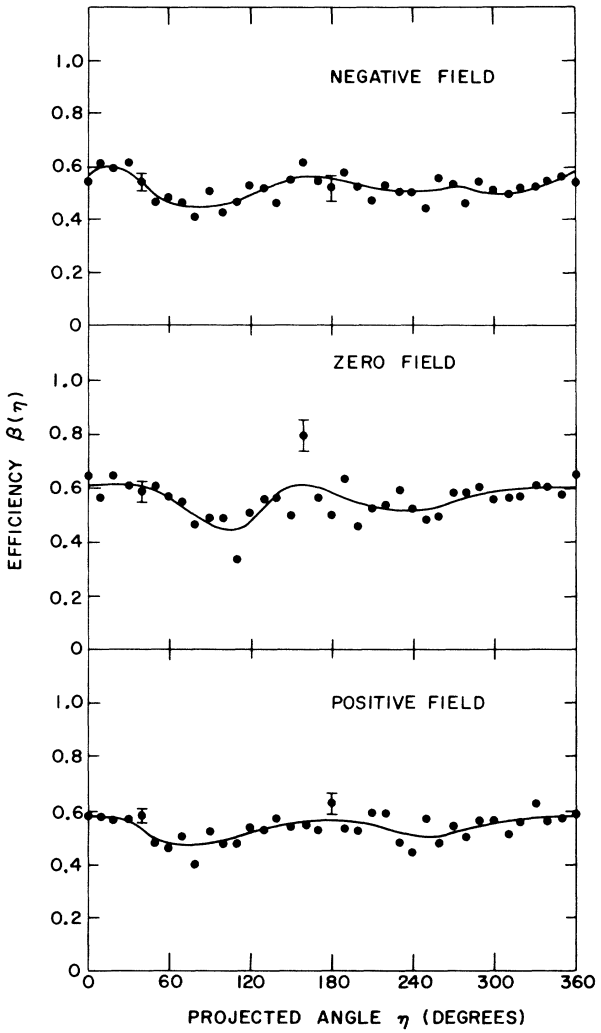

FIG. 14. Efficiency functions of the NBT events for the three field configurations calculated using 20 000 Monte Carlo events. The dots are the raw efficiency values and the curves are the results from the smoothing procedure described in the text.

TABLE I. Fourier coefficients of efficiency function.

Sample	Field	a_0	a_1	δ_1 (deg)
All events	−	0.804	0.071	167
	0	0.830	0.081	175
	+	0.816	0.074	174
Nonbeam tube (NBT)	−	0.523	0.013	136
	0	0.562	0.027	119
	+	0.538	0.016	155
NBT, $R_V > 4.0$ cm	−	0.413	0.017	97
	0	0.454	0.013	102
	+	0.424	0.015	29
NBT, $R_V > 4.5$ cm	−	0.314	0.009	70
	0	0.324	0.012	103
	+	0.333	0.014	3
NBT, $R_V > 5.0$ cm	−	0.223	0.005	10
	0	0.217	0.011	155
	+	0.245	0.011	−24
NBT, $R_V > 5.5$ cm	−	0.150	0.006	24.5
	0	0.139	0.009	−155.1
	+	0.177	0.006	−26.7
NBT, $R_V > 6.0$ cm	−	0.105	0.006	27.9
	0	0.074	0.002	165.6
	+	0.125	0.002	44.9

III D 4, this means that the maximum-likelihood analysis is not sensitive to the choice of efficiency function. The efficiency functions remained essentially unchanged whether the Fermi momentum of the target neutron was included in the Monte Carlo calculation or not.

Comparison of the Monte Carlo event distributions with those of the data that were displayed in Figs. 9–13 showed in general good agreement with the data. The Λ-decay vertex position distribution agreed and showed the accepted Λ lifetime. The loss of events near the beginning and the end of the chamber was due to scanning inefficiency in these regions. The tails in the Λ momentum distribution were due to neglecting the beam divergence and momentum spread in the Monte Carlo calculation and to events that had no range measured. The opening angle and π^- center-of-mass angular distributions showed loss at small angles due to the rejected ambiguous events and a loss at large angles due to spark-chamber and scanning inefficiencies.

3. *Fits to Projected-Angle Distributions*

Three histograms were set up, one for each field configuration, which were divided into 10° bins in projected angle. Each histogram was fitted to a function of the form

$$f(\eta) = N_0[1 + K\cos(\eta - \epsilon)]\beta(\eta),$$

where

$$K \equiv \tfrac{1}{4}\pi\langle\alpha\overline{P}\rangle,$$

to determine the average asymmetry and precession angle of the distribution. Then using the mean value of the ratio $\int \vec{H}\cdot d\vec{l}/p_\Lambda$ for that sample the Λ magnetic moment was calculated using Eq. (5′).

The histogram-fitting program was checked using events generated in the Monte Carlo calculation. First, the originally generated events were fitted without bias. Second, the accepted events were fitted using either the raw or smoothed efficiency function. In all of these cases the best-fit parameters agreed with those used in generating the events.

Several subsets of the data and several choices of efficiency function were tried. The results of the fitting are summarized in Table II. The sample of all accepted events including small-angle Λ's going through the beam tube showed some internal inconsistencies. Since these events were expected to have the largest bias and the Λ could have interacted in the beam tube, only the NBT events that had the Λ missing the beam tube were used for the final analysis. There were a total of 4291 such NBT events of which 1675 events had negative field, 2193 events had positive field, and 423 events had zero field.

Figure 15 shows histograms for all the NBT events and the best fits to them. Fitting with the smoothed efficiency function rather than the raw one had little effect on the fitted parameters but did improve the χ^2 for the fits. Even if the "reversed" biases were used, i.e., using the bias generated with a positive field when fitting the negative-field data and vice versa, the magnetic moment changed by about $0.12\mu_N$. Since this is equivalent to a change of $1.50\mu_N$ in the Monte Carlo calculation, the results were not very sensitive to the choice of the efficiency function. The effect of removing those events with the Λ-decay vertex near the beam tube was investigated. The results did not show any systematic effects as a function of the vertex radius cut R_V, which showed that the biases in the events had been corrected and that the entire NBT sample could be used. This gave an average decay asymmetry $\langle\alpha\overline{P}\rangle = 0.608 \pm 0.024$ and a Λ magnetic moment $\mu_\Lambda = (-0.73 \pm 0.17)\mu_N$ with a χ^2 of 77.4 for 70 degrees of freedom. The asymmetry for the positive-field data, however, was consistently smaller than that of the zero- and negative-field data.

Because this method of fitting the projected-angle distribution used only the average $\int \vec{H}\cdot d\vec{l}/p_\Lambda$, it was insensitive to mismeasurements of the momentum of an individual event. A systematic error in determining p_Λ would, of course, lead to an error in the magnetic moment. This and other systematic effects will be discussed in Sec. III D 5.

4. *Maximum-Likelihood Analysis*

The second method used to extract the decay asymmetry and magnetic moment from the data was the maximum-likelihood technique. Using Eq. (15), the probability for event i to have the measured projected angle η_i is

$$f_i(\eta_i; K, \mu_\Lambda) = \mathfrak{N}_i(K, \mu_\Lambda)\beta(\eta_i)[1 + K\cos(\eta_i - \gamma_i\mu_\Lambda)], \tag{18}$$

where

$$\mathfrak{N}_i(K, \mu_\Lambda) = [2\pi a_0 + \pi a_1 K\cos(\delta_1 - \gamma_i\mu_\Lambda)]^{-1}$$

and

$$\gamma_i \equiv -e(m_\Lambda/m_p)\left(\int \vec{H}\cdot d\vec{l}/p_\Lambda\right)_i. \tag{19}$$

Letting $\beta_i' = \beta(\eta_i)/(2\pi a_0)$ and $B_1 = a_1/(2a_0)$, Eq. (18) becomes

$$f_i(\eta_i; K, \mu_\Lambda) = \beta_i' N_i D_i^{-1}, \tag{20}$$

where

TABLE II. Fits to projected-angle distributions.

Sample	Bias	$\langle \int \vec{H} \cdot d\vec{l}/p_\Lambda \rangle$ [kG cm/(GeV/c)]	No. of events	$\langle \alpha \bar{P} \rangle$	ϵ (deg)	χ^2/34 d.f.	Over-all fit $\langle \alpha \bar{P} \rangle$	Over-all fit $\langle \mu_\Lambda \rangle$ (μ_N)
All events	Raw	−799	2164	0.658 ± 0.034	−12.0 ± 3.4	34.6	0.592 ± 0.022	−0.69 ± 0.16
		0	532	0.682 ± 0.069	8.9 ± 6.3	35.2		
		789	2686	0.519 ± 0.031	9.9 ± 3.9	50.3		
NBT	Raw	−810	1675	0.653 ± 0.039	−12.0 ± 3.8	34.6	0.588 ± 0.025	−0.73 ± 0.17
		0	423	0.654 ± 0.080	13.3 ± 7.4	47.6		
		796	2193	0.524 ± 0.035	12.0 ± 4.2	40.1		
	Smooth	−810	1675	0.653 ± 0.039	−12.0 ± 3.8	30.7	0.588 ± 0.025	−0.73 ± 0.17
		0	423	0.654 ± 0.080	13.3 ± 7.4	42.6		
		796	2193	0.524 ± 0.035	12.0 ± 4.2	40.7		
	Reverse	−810	1675	0.655 ± 0.031	−11.0 ± 3.8	28.5	0.589 ± 0.025	−0.66 ± 0.17
		0	423	0.654 ± 0.080	13.3 ± 7.4	42.6		
		796	2193	0.517 ± 0.035	10.8 ± 4.3	36.2		
NBT, Type 2, 3	Smooth	−792	1256	0.623 ± 0.045	−12.7 ± 4.7	23.2	0.613 ± 0.028	−0.73 ± 0.19
		0	324	0.632 ± 0.090	9.6 ± 9.0	29.8		
		785	1707	0.602 ± 0.038	10.8 ± 4.2	49.8		
NBT, $0.40 \leq p_\Lambda \leq 0.80$	Smooth	−794	1523	0.698 ± 0.040	−14.3 ± 3.7	31.2	0.627 ± 0.025	−0.77 ± 0.17
		0	384	0.695 ± 0.082	11.0 ± 7.3	40.7		
		785	2023	0.558 ± 0.036	10.0 ± 4.1	37.7		
NBT, $R_V > 4.0$ cm	Smooth	−817	1488	0.661 ± 0.042	−12.3 ± 4.0	35.0	0.587 ± 0.027	−0.67 ± 0.18
		0	377	0.670 ± 0.084	15.4 ± 7.6	37.5		
		800	1957	0.513 ± 0.037	9.5 ± 4.6	37.8		
NBT, $R_V > 4.5$ cm	Smooth	−823	1288	0.672 ± 0.044	−10.8 ± 4.2	26.8	0.591 ± 0.028	−0.59 ± 0.19
		0	345	0.680 ± 0.088	17.0 ± 7.8	41.5		
		806	1693	0.506 ± 0.040	8.4 ± 5.0	33.9		
NBT, $R_V > 5.0$ cm	Smooth	−835	1066	0.682 ± 0.048	−9.5 ± 4.5	28.9	0.628 ± 0.030	−0.63 ± 0.20
		0	295	0.683 ± 0.095	24.4 ± 8.3	46.2		
		807	1413	0.574 ± 0.043	12.0 ± 4.8	26.0		
NBT, $R_V > 5.5$ cm	Smooth	−841	864	0.684 ± 0.054	−11.4 ± 5.0	32.6	0.640 ± 0.034	−0.79 ± 0.21
		0	245	0.712 ± 0.101	25.7 ± 8.7	50.1		
		814	1139	0.589 ± 0.048	15.4 ± 5.1	31.2		
NBT, $R_V > 6.0$ cm	Smooth	−844	657	0.675 ± 0.061	−10.9 ± 5.8	39.3	0.617 ± 0.038	−0.81 ± 0.25
		0	192	0.606 ± 0.118	28.9 ± 11.9	53.7		
		819	886	0.574 ± 0.054	16.9 ± 6.0	35.8		

$$N_i \equiv 1 + K\cos(\eta_i - \gamma_i \mu_\Lambda),$$

$$D_i \equiv 1 + B_1 K\cos(\delta_1 - \gamma_i \mu_\Lambda).$$

The likelihood function for a sample of N events is the product of the probabilities for each event,

$$\mathfrak{L} = \prod_{i=1}^{N} f_i(\eta_i; K, \mu_\Lambda)$$

and

$$w \equiv \ln\mathfrak{L} = \sum_{i=1}^{N} (\ln\beta_i' + \ln N_i - \ln D_i).$$

The values of K and μ_Λ are determined by maximizing the likelihood at which the derivatives of w vanish,

$$\begin{aligned}\frac{\partial w}{\partial \mu_\Lambda} &= \sum_{i=1}^{N}\left(\frac{1}{N_i}\frac{\partial N_i}{\partial \mu_\Lambda} - \frac{1}{D_i}\frac{\partial D_i}{\partial \mu_\Lambda}\right)\\ &= \sum_{i=1}^{N}\gamma_i K\left(\frac{\sin(\eta_i - \gamma_i\mu_\Lambda)}{1 + K\cos(\eta_i - \gamma_i\mu_\Lambda)} - \frac{B_1\sin(\delta_1 - \gamma_i\mu_\Lambda)}{1 + B_1 K\cos(\delta_1 - \gamma_i\mu_\Lambda)}\right)\\ &= 0,\end{aligned} \tag{21}$$

$$\begin{aligned}\frac{\partial w}{\partial K} &= \sum_{i=1}^{N}\left(\frac{1}{N_i}\frac{\partial N_i}{\partial K} - \frac{1}{D_i}\frac{\partial D_i}{\partial K}\right)\\ &= \sum_{i=1}^{N}\left(\frac{\cos(\eta_i - \gamma_i\mu_\Lambda)}{1 + K\cos(\eta_i - \gamma_i\mu_\Lambda)} - \frac{B_1\cos(\delta_1 - \gamma_i\mu_\Lambda)}{1 + B_1 K\cos(\delta_1 - \gamma_i\mu_\Lambda)}\right)\\ &= 0.\end{aligned}$$

These are a pair of simultaneous nonlinear equations which may be solved for K and μ_Λ by standard iterative methods. Note that this way of analyzing the data weights those events that have high field integral and/or low momentum more strongly. Furthermore, since B_1 is small, this method is also insensitive to the choice of the bias function.

Several checks were made on the maximum-likelihood program. First, for a sample of 6400 Monte Carlo events generated with $\langle\alpha\bar{P}\rangle = 0.69$ and $\mu_\Lambda = -0.75\mu_N$, the program gave $\langle\alpha\bar{P}\rangle = 0.71 \pm 0.02$ and $\mu_\Lambda = (-0.73 \pm 0.12)\mu_N$. Second, by assigning to each event in the data the average measured value of $\int \vec{H}\cdot d\vec{l}/p_\Lambda$ instead of its individual measured value, the program should give the same results as obtained from the projected-angle fitting. This was verified for one data sample.

The results of the maximum-likelihood analysis for several subsets of the data are displayed in Table III. The asymmetry parameter is in good agreement with that derived from the projected-angle fits, but the Λ magnetic moment has been shifted by about $0.16\mu_N$ for the data of all types and by $0.08\mu_N$ for these events having at least one range measured.

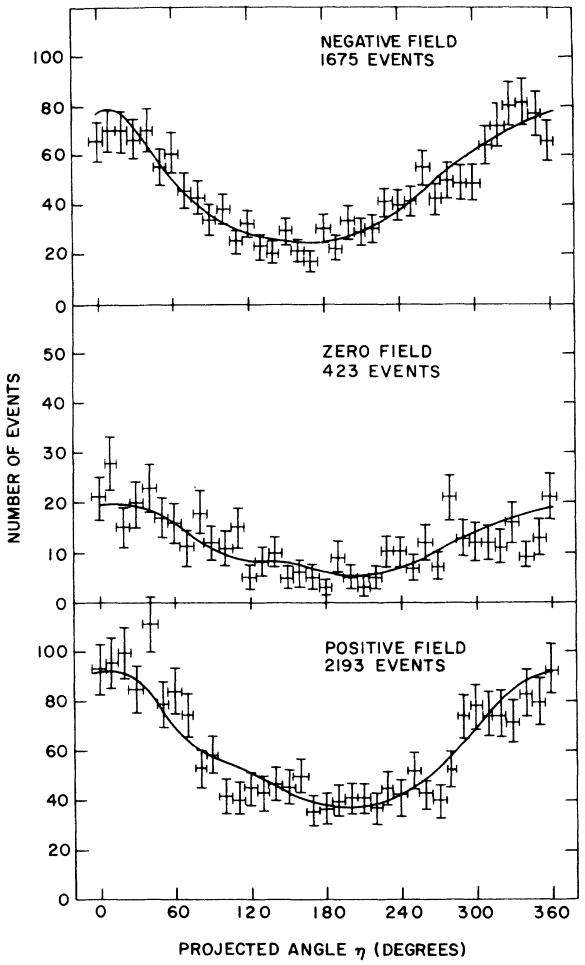

FIG. 15. Projected-angle distribution of the NBT events for the three field configurations. The smooth curves are the best fits using Eq. (15).

To check the effects of errors in determining the Λ momentum on the maximum-likelihood calculation, a sample of the Monte Carlo events was analyzed in the following manner. Assigning to each event a value of $\int \vec{H}\cdot d\vec{l}/p_\Lambda$ chosen randomly from a normal distribution having the same mean and variance as the experimental data (the means of the distributions of this ratio were equal within ~0.5% for the experimental data and the Monte Carlo sample), the program, however, gave the results $\langle\alpha\bar{P}\rangle = 0.71 \pm 0.02$ and $\mu_\Lambda = -0.67 \pm 0.12\mu_N$, a decrease of $0.06\mu_N$. This effect can also be estimated as follows: Ignoring the term due to the efficiency function and assuming K is known, Eq. (21) can be expanded to first order in $\gamma_i\mu_\Lambda$ and solved for μ_Λ:

$$\mu_\Lambda = \sum_{i=1}^{N}\gamma_i c_i \Big/ \sum_{i=1}^{N}\gamma_i^2 d_i, \tag{22}$$

TABLE III. Maximum-likelihood analysis.

Sample	No. of events[a]	$\langle\alpha\bar{P}\rangle$	μ_Λ (μ_N)
All events	5382	0.588 ± 0.022	−0.56 ± 0.16
Nonbeam tube (NBT)	4291	0.583 ± 0.025	−0.57 ± 0.17
NBT, Type 2 and 3	3287	0.613 ± 0.028	−0.64 ± 0.19
NBT, $R_V > 4.0$ cm	3822	0.580 ± 0.027	−0.50 ± 0.18
NBT, $R_V > 4.5$ cm	3326	0.582 ± 0.028	−0.44 ± 0.19
NBT, $R_V > 5.0$ cm	2774	0.615 ± 0.030	−0.50 ± 0.20
NBT, $R_V > 5.5$ cm	2248	0.622 ± 0.034	−0.64 ± 0.22
NBT, $R_V > 6.0$ cm	1735	0.590 ± 0.039	−0.65 ± 0.26

[a]Includes zero-field events.

where

$$c_i \equiv \sin\eta_i/(1+K\cos\eta_i)\,,$$

$$d_i \equiv (K+\cos\eta_i)/(1+K\cos\eta_i)^2\,.$$

Thus if γ_i are normally distributed with a mean $\langle\gamma\rangle$ and variance σ^2, Eq. (22) becomes

$$\mu_\Lambda = \langle\gamma\rangle \sum_{i=1}^{N} c_i \Big/ \sum_{i=1}^{N} d_i(\langle\gamma\rangle^2+\sigma^2)$$

$$\simeq \langle\mu_\Lambda\rangle[1-(\sigma/\langle\gamma\rangle)^2]\,, \qquad (23)$$

where $\langle\mu_\Lambda\rangle$ is the value of the magnetic moment calculated assuming $\gamma_i = \langle\gamma\rangle$. From the experimental data, $\sigma/\langle\gamma\rangle \simeq 200/800$ which gives a shift of about $0.05\mu_N$. These estimates of the shift are smaller than the effect in the experimental data because the observed $\int \vec{H}\cdot d\vec{l}/p_\Lambda$ distribution was skewed toward high value as shown in Fig. 16.

Since there is this discrepancy between the two ways of analyzing the data, it was concluded that the maximum-likelihood method was not suitable in this experiment because of the uncertainty in determining the Λ momentum in each individual event. Therefore, the best value for the Λ magnetic moment is that given by fitting the projected-angle distributions.

5. *Systematic Effects*

The error in the final result of μ_Λ is purely statistical. There were, however, several possible sources of systematic effects.

1. Fringe field. The decay p and π^- tracks were in principle curved because of the fringe field, and the low-momentum π^- was affected more than the p. Moreover, this curving gave a systematic rotation of the decay plane, e.g., a positive field would give the π^- track a right-handed rotation independent of the Λ direction. This curving was minimized by measuring the tangent line of the track at the decay vertex. The effect was estimated by a Monte Carlo calculation to make μ_Λ apparently more negative by ≲3%.

2. Production-vertex distribution. Due mainly to the short mean life of the Λ, the average production vertex was shifted downstream from the center of the target. This resulted in an overestimate on the field integral using Eq. (10) and was estimated from the Monte Carlo calculation to make μ_Λ more negative by ≲1.5%.

3. Uncertainty in p_Λ determination. As compared with the Monte Carlo results, the data showed an average p_Λ of about 2.5% low. In the Monte Carlo program, the Λ mean life used was about 4% too high and the beam spreads were neglected. These led to opposite shifts in the average p_Λ. There was also the possibility of slightly underestimating the

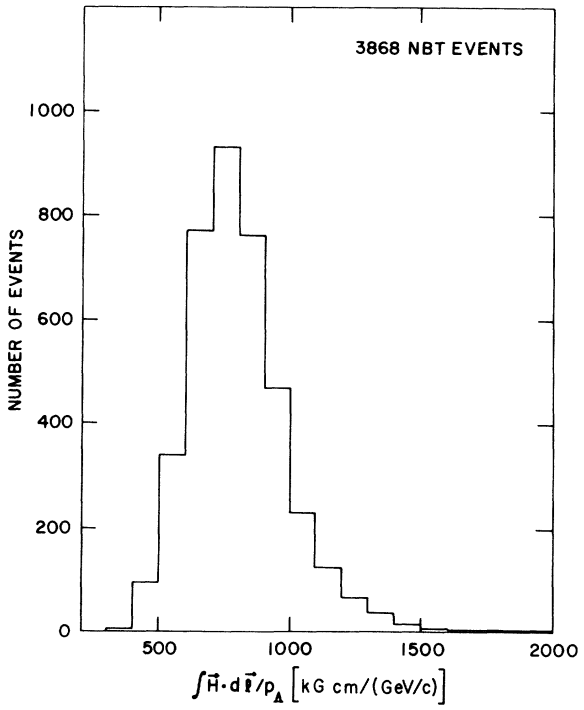

FIG. 16. Distribution of $\int \vec{H}\cdot d\vec{l}/p_\Lambda$ for the NBT events, both field polarities combined.

p and/or π^- momentum if they stopped close to the chamber walls. This would lead to an overestimate on the magnitude of μ_Λ by $\lesssim 2.5\%$.

4. Efficiency function. As mentioned earlier, the result had but very weak dependence on the correct choice of the efficiency function $\beta(\eta)$, i.e., the correct choice of parameters in the Monte Carlo program which generated $\beta(\eta)$ was not critical. The result of an upper-limit estimation of the effect that the uncertainty in $\beta(\eta)$ has on μ_Λ is to make the error in μ_Λ about 5% larger, making the statistical uncertainty of the experiment to be $0.18\mu_N$. However, it correlated the errors on $\alpha\overline{P}$ and μ_Λ. The correlation coefficients were found to be $\lesssim 3\%$.

Since these effects are small, they have not been included in the quoted result.

IV. DISCUSSION OF RESULTS

The results of the different measurements of the Λ magnetic moment are listed in Table IV. As they agree statistically rather well, a weighted average and its error are also included.

Different values of the Λ magnetic moment have been predicted based on various strong-interaction models.[1] Under the current unitary symmetry scheme, there have been several models discussed. The Sakata model, in which (p, n, Λ) forms the basis of a three-dimensional representation of the SU_3 group while other baryons belong to a higher-dimensional representation, predicts the Λ magnetic moment to be equal to that of the neutron,[2] $\mu_\Lambda = \mu_n = -1.91\mu_N$. The Gell-Mann–Ne'eman scheme (eightfold way) in which the baryons and mesons form the basis of the eight-dimensional representation of the SU_3 group gives $\mu_\Lambda = \frac{1}{2}\mu_n$.[3] The model of Gürsey *et al.*,[4] assuming that the baryons and mesons are bound states of some assumed triplets which transform according to the three-dimensional representations of the SU_3 group, predicts $\mu_\Lambda = \frac{5}{6}\mu_n$ [Ref. 5] if the charge of the triplet is (1, 2, 1) in units of electron charge. However, it gives the same prediction as the "eightfold way" if the triplet of quarks has charge $(-\frac{1}{3}, \frac{2}{3}, -\frac{1}{3})$. By expanding to SU_6, Bég *et al.*[6] have predicted the magnetic moment of the neutron in terms of that of the proton, in agreement with observed value to within a few percent. As a result, the prediction for μ_Λ is essentially the same as in the SU_3 quark model. When the mass difference between the baryons is taken into account,[6] the prediction becomes $\mu_\Lambda = -0.78\mu_N$. More recently, using the technique of current algebra, Mathur and Pandit[7] predicted $\mu_\Lambda = -0.75\mu_N$. Further discussions of models which lead to relationships between the baryon magnetic moments can be found in the papers of Cheng and Pagels,[8] and Franklin.[9]

The result of this experiment $\mu_\Lambda = (-0.73 \pm 0.18)\mu_N$ is in excellent agreement with the "mass-corrected" value and the result using current algebra, and is within 1.5 standard deviations of the SU_3 prediction based on octets or quarks. The result, however, is inconsistent with the predictions of the Sakata model and the integral-charged triplet model.

The Σ^+ magnetic moment which has the same prediction from SU_3 and the integral-charged triplet model has been measured several times with an average result of $(2.57 \pm 0.52)\mu_N$.[16] It cannot differentiate the SU_3 and the "mass-corrected" predictions because of the large uncertainty. It is clear that in order to further differentiate between the theoretical models, measurements on the hyperon magnetic moments should be made with greater accuracy. In general, accurate magnetic-moment measurement on only one of the hyperons is needed to differentiate between certain models, but, in order to test a model more completely, measurement has to be made on several hyperons and perhaps on members of the other multiplets. The major diffi-

TABLE IV. Summary of measurements of the Λ magnetic moment.[a]

Experiment	Detector	No. of events	Magnetic moment (μ_N)
Cool *et al.*[b]	Spark chamber	254	-1.5 ± 0.5
Kernan *et al.*[c]	Cloud chamber	20	0.0 ± 0.6
Anderson and Crawford[d]	H_2 bubble chamber	8553	-1.39 ± 0.72
Charrier *et al.*[e]	Emulsion	151	-0.5 ± 0.28
This experiment	Spark chamber	3868	-0.73 ± 0.18
Average			-0.72 ± 0.16

[a] *Note added in proof.* The CERN emulsion group has recently published their result of $\mu_\Lambda = (-0.73 \pm 0.07)\mu_N$ (Ref. 26).

[b] Reference 17.

[c] Reference 18.

[d] Reference 19.

[e] Reference 20.

culty in this experiment was the high instantaneous rates mainly due to using a pulsed magnet. With recent improvements in experimental techniques, and especially high-field superconducting magnets, better measurements of the hyperon magnetic moments are becoming feasible.

ACKNOWLEDGMENTS

We wish to thank Dr. R. L. Cool for his interest and useful discussions. The magnet was designed and tested at MIT with the help of Dr. H. Brechna. Professor J. Friedman and Dr. E. Loh contributed to the design and Dr. A. B. Clegg aided in the preliminary state of the experiment. We are indebted to Dr. E. O. Salant and Dr. R. P. Shutt and their groups for providing us with film-measuring equipment. We also wish to thank the cosmotron staff for their cooperation. The technical assistance of E. Druek, G. Munoz, H. Sauter, F. Seier, and O. Thomas and the untiring efforts of our scanners M. Zeitlin, M. L. Montecalvo, B. Job, and R. Arata are greatly appreciated.

---

*Work done under the auspices of the U. S. Atomic Energy Commission and supported in part with funds provided under Contract No. AT(30-1)2098.

†Present address: Vitro Laboratories, Silver Spring, Md.

‡Present address: Brookhaven National Laboratory, Upton, N.Y.

§Present address: Department of Physics, University of Arizona, Tucson, Ariz.

‖Present address: Department of Physics, University of California at San Diego, La Jolla, Calif.

[1]H. Katsumori, Progr. Theoret. Phys. (Kyoto) 18, 375 (1957); B. T. Feld and G. Costa, Phys. Rev. 110, 968 (1958); W. G. Holladay, *ibid.* 115, 1331 (1959); K. Tanaka, *ibid.* 122, 705 (1961); S. N. Biswas, *ibid.* 127, 1350 (1962).

[2]S. Okubo, Progr. Theoret. Phys. (Kyoto) 27, 949 (1962); N. Cabibbo and R. Gatto, Nuovo Cimento 21, 872 (1961).

[3]S. Coleman and S. L. Glashow, Phys. Rev. Letters 6, 423 (1961).

[4]F. Gürsey, T. D. Lee, and M. Nauenberg, Phys. Rev. 135, B467 (1964).

[5]M. Nauenberg, Phys. Rev. 135, B1047 (1964).

[6]M. A. B. Bég and A. Pais, Phys. Rev. 137, B1514 (1965).

[7]V. S. Mathur and L. K. Pandit, Phys. Rev. 147, 965 (1966).

[8]T. P. Cheng and H. Pagels, Phys. Rev. 172, 1635 (1968).

[9]J. Franklin, Phys. Rev. 182, 1607 (1969).

[10]M. Goldhaber, Phys. Rev. 101, 1828 (1956).

[11]T. D. Lee and C. N. Yang, Phys. Rev. 108, 1645 (1957).

[12]F. S. Crawford, in *Proceedings of the 1962 International Conference on High Energy Physics at CERN*, edited by J. Prentki (CERN, Geneva, 1962), p. 270.

[13]B. Cork, L. Kerth, W. A. Wenzel, J. W. Cronin, and R. L. Cool, Phys. Rev. 120, 1000 (1960).

[14]See R. Hagedorn, *Relativistic Kinematics* (Benjamin, New York, 1963) for further references.

[15]T. D. Lee, J. Steinberger, G. Feinberg, P. K. Kabir, and C. N. Yang, Phys. Rev. 106, 1367 (1957). Under our sign convention the proton helicity from Λ decay is $-\alpha$.

[16]Particle Data Group, Rev. Mod. Phys. 42, 87 (1970).

[17]R. L. Cool, E. W. Jenkins, T. F. Kycia, D. A. Hill, L. Marshall, and R. A. Schluter, Phys. Rev. 127, 2223 (1962).

[18]W. Kernan, T. B. Novey, S. D. Warshaw, and A. Wattenberg, Phys. Rev. 129, 870 (1963).

[19]J. A. Anderson and F. S. Crawford, Phys. Rev. Letters 13, 167 (1964).

[20]G. Charriere, M. Gailloud, Ph. Rosselet, R. Weill, W. M. Gibson, K. Green, P. Tolun, N. A. Whyte, J. C. Combe, E. Dahl-Jensen, N. T. Doble, D. Evans, L. Hoffmann, W. T. Toner, H. Göing, K. Gottstein, W. Püschel, V. Scheuing, and J. Tietge, Phys. Letters 15, 66 (1965); G. Charriere, Helv. Phys. Acta 42, 339 (1969).

[21]D. A. Hill, K. K. Li, E. W. Jenkins, T. F. Kycia, and H. Ruderman, Phys. Rev. Letters 15, 85 (1965).

[22]L. Marshall, Rev. Sci. Instr. 33, 919 (1962).

[23]L. Tepper, G. L. Miller, and T. F. Kycia, IEEE Trans. Nucl. Sci. NS-11, 431 (1964).

[24]H. Brechna, D. A. Hill, and B. M. Bailey, Rev. Sci. Instr. 36, 1529 (1965).

[25]R. Sugarman, F. C. Merritt, and W. A. Higinbotham, Brookhaven National Laboratory Manual No. BNL 711 (T-248) (unpublished).

[26]E. Dahl-Jensen, N. Doble, D. Evans, A. J. Herz, U. Liebermeister, Ph. Rosselet, C. Busi, G. Önengüt, P. Tolun, M. Gailloud, R. Weill, G. Hansl, A. Manz, W. Püschel, R. Settles, G. Baroni, G. Romano, and V. Rossi, Nuovo Cimento 3A, 1 (1971).

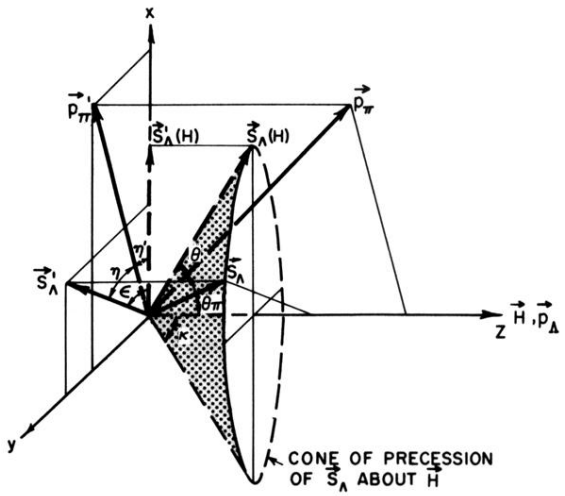

FIG. 13. Definition of angles in Λ rest frame used in analysis.

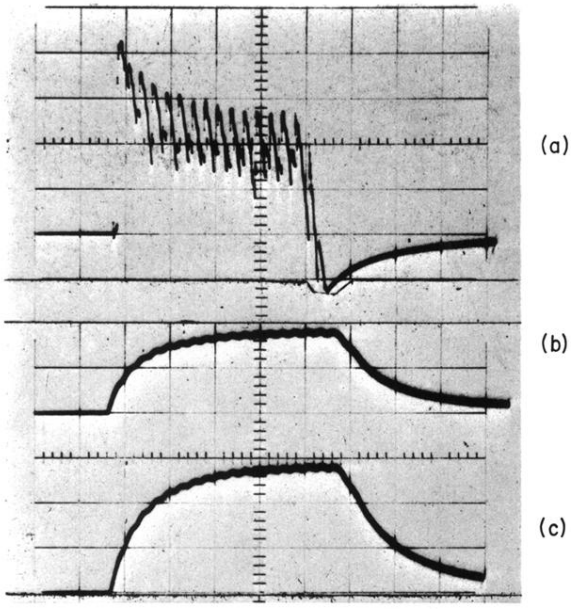

FIG. 3. Magnet pulse wave forms: (a) voltage pulse, (b) current pulse, and (c) field integral along core surface (horizontal scale: 1 msec/div).

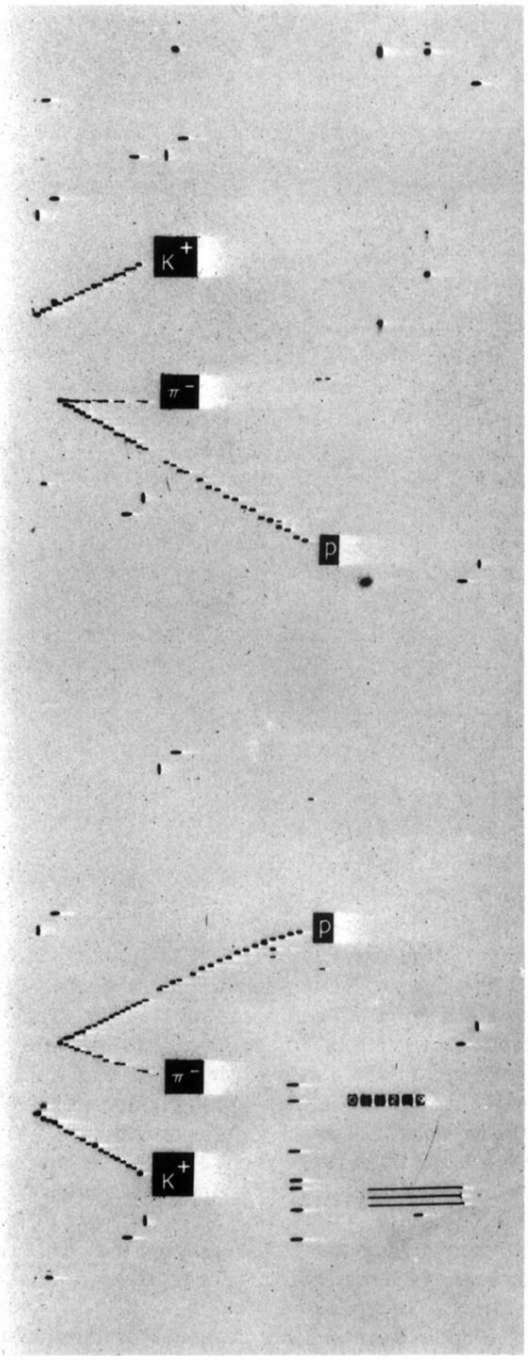

FIG. 8. A typical Λ event.